Nano Research
2022, 15(12): 10021–10028

ISSN 1998-0124 CN 11-5974/O4
https://doi.org/10.1007/s12274-022-5094-8

Research Article

Constructing hierarchical nanosheet-on-microwire FeCo LDH@Co_3O_4 arrays for high-rate water oxidation

Tang Tang[1,2], Zhe Jiang[1,2], Jun Deng[3], Shuai Niu[1,2], Ze-Cheng Yao[1,2], Wen-Jie Jiang[1], Lin-Juan Zhang[4,5], and Jin-Song Hu[1,2,5] (✉)

[1] *Beijing National Laboratory for Molecular Sciences (BNLMS), CAS Key Laboratory of Molecular Nanostructure and Nanotechnology, Institute of Chemistry, Chinese Academy of Sciences, Beijing 100190, China*
[2] *University of the Chinese Academy of Sciences, Beijing 100049, China*
[3] *Beijing National Laboratory for Condensed Matter Physics, Institute of Physics, Chinese Academy of Sciences, Beijing 100190, China*
[4] *Shanghai Synchrotron Radiation Facility, Shanghai Institute of Applied Physics, Chinese Academy of Sciences, Shanghai 201800, China*
[5] *Dalian National Laboratory for Clean Energy, Dalian 116023, China*

Received: 29 May 2022 / **Revised:** 13 August 2022 / **Accepted:** 24 September 2022

ABSTRACT

Alkaline electrochemical water oxidation powered by renewable energies is a promising and environmentally friendly way to produce hydrogen. The industrial water electrolyzers are commonly operated at a high current density, calling for abundant and durable active sites to participate in. The rational design of hierarchically structured electrocatalysts is thus essential to industrial water electrolyzers. Herein, we develop a Fe^{3+} induced nanosizing strategy for fabricating such a hierarchical FeCo LDH@Co_3O_4 (LDH: layered double hydroxide) nanostructure array for high-rate water oxidation. Density functional theory (DFT) simulations indicate that the introduction of Fe^{3+} with a small ion radius and high electrical repulsion in the LDH layer distorted the LDH layer, resulting in a reduced nanosheet size and enabling the formation of a hierarchical structure. Such structure cannot be achieved without the participation of Fe^{3+} cations. Benefiting from the significantly enhanced electrochemical surface areas and charge/mass transport due to the hierarchical structure together with the boosted intrinsic activity by electronic modulation of Fe^{3+}, such FeCo LDH@Co_3O_4 electrode can deliver an industrial-level current density of 1,000 mA·cm^{-2} at a small overpotential of 392 mV for water oxidation. When assembled in a water electrolyzer, it delivers a current density of 100 mA·cm^{-2} at a low operation voltage of 1.61 V. Powered by solar light, the electrolyzer demonstrates high solar-to-hydrogen efficiency of 18.15% with stable and reproducible photoresponse. These results provide new insights for constructing hierarchical nanostructures for advanced water oxidation and other diverse applications.

KEYWORDS

electrocatalysts, oxygen evolution reaction, water splitting, hierarchical structures, layered double hydroxides

1 Introduction

The burgeoning energy demand of modern society calls for the exploitation of green and sustainable energy conversion and storage technologies [1–4]. Owing to the high energy density of ~ 120 MJ·kg^{-1} and the advantages of zero-carbon emission, hydrogen has been considered a promising alternative energy source for the current fossil fuels [5–7]. Developing sustainable hydrogen production ways is essential in hydrogen economics. Alkaline water electrolysis powered by renewable energies is a promising and environmentally friendly way to produce hydrogen [8]. However, the major challenge resides in the sluggish kinetics and thus large overpotentials of the anode oxygen evolution reaction (OER) [9–12], which traditionally relies on the use of platinum group metal (PGM) such as Ru- and Ir-based catalysts [13, 14]. The PGM catalysts commonly come up with the expense of high cost and limited durability [15]. Therefore, rational fabrication of high-efficiency OER catalysts based on earth-abundant materials is of great importance for the practical utilization of water electrolysis for renewable hydrogen production [16, 17].

Commonly, industrial water electrolyzers (WEs) are commonly operated at a high current density larger than 200 mA·cm^{-2} [18–20]. As a typical gas-involved reaction, the OER predominantly occurs at the three-phase interface of solid-phase catalytic centers, liquid-phase electrolytes, and gas-phase oxygen, leaving the active sites only at the interface accessible and functional [21, 22]. Therefore, high-performance electrocatalysts for industrial WEs require an advanced architecture with abundant accessible and durable electrocatalytic active sites [9, 23–25]. Despite this requirement, the rational design of electrode architectures has received insufficient attention. The electrode fabricated by coating powdery materials with inactive and insulating polymeric binders usually results in not only limited charge/mass transport but also performance decay due to the mechanical catalyst shedding [26–28]. In contrast, *in-situ* growth of binder-free hierarchical nano/microstructures with delicately designed morphologies as an integrated electrode has shown

---

Address correspondence to hujs@iccas.ac.cn

many advantages [22, 29, 30], such as increased accessible active sites, enhanced electron/mass transportation, and facilitated gas release, etc. [26].

Among various non-PGM alternatives, layered double hydroxides (LDHs) are regarded as promising OER catalysts for their superior stability in alkaline media [4, 31–36]. However, their activities still need to be improved, especially at a large current output given their insufficient exposed active sites and electrical conductivity [37–39]. A couple of strategies have been developed to enhance the electrocatalytic performance of LDHs, including heteroatoms doping, phase engineering, etc. [40–43]. Nevertheless, the fabrication of hierarchically nanostructured LDH electrodes with those above-mentioned merits, improved intrinsic activities and charge transportation still remains challenging and is worthy of further investigation for the potential application in industrial WEs.

Herein, we discovered a trivalent Fe^{3+} induced nanosizing strategy for fabricating a hierarchical binary FeCo LDH@Co_3O_4 nanostructure arrays with abundant highly active and durable catalytic sites for high-rate water oxidation. It featured FeCo LDH nanosheet arrays assembled on Co_3O_4 microwire arrays which were densely grown on a nickel foam substrate (the catalyst was thus denoted as FeCo LDH@Co_3O_4/NF, where NF is nickel foam). It was found that the Fe^{3+} substitution not only activated Co sites to boost intrinsic activity but also significantly reduced the nanosheet size of LDHs, enabling the formation of the hierarchical structure of nanosheet arrays on microwires. Such architecture could not be achieved with no introduction of Fe^{3+} cations (route 1 in Fig. 1). The resulting hierarchical electrode features various advantages: (1) Each Co_3O_4 microwire was grown tightly on the current collector (NF) with superior mechanical stability and electrical contact, building up an expressway for charge transfer during the reaction; (2) the densely grown FeCo LDH nanosheet substructure held not only favorably modulated electronic structure for enhanced intrinsic activity but also enlarged surface to accommodate more accessible OER sites; (3) the macropores of NF and open spacing between neighboring microwires offered facile electrolyte penetration and mass transport; and (4) the chemical durable FeCo LDH together with mechanical durable binder-free architecture ensured the overall robust durability. These features gave FeCo LDH@Co_3O_4/NF a superior OER kinetic and long operation life. It could deliver an OER current density of 10 $mA\cdot cm^{-2}$ at a small overpotential of 226 mV or 1,000 $mA\cdot cm^{-2}$ at 392 mV. When assembled in a WE, the current density of 100 $mA\cdot cm^{-2}$ could be achieved at a low operation voltage of 1.61 V. Powered by solar light, the WE demonstrated an attractive solar-to-hydrogen efficiency of 18.15% with reproducible photoresponse.

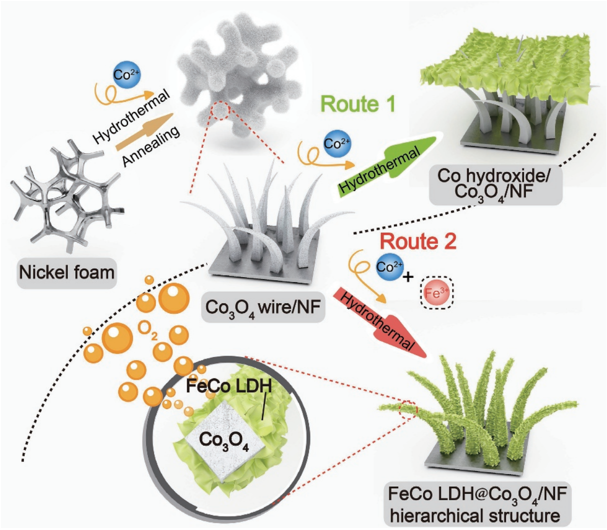

Figure 1 Schematic synthesis of FeCo LDH@Co_3O_4/NF hierarchical structure.

2 Experimental section

Chemical and materials: Cobalt(II) nitrate hexahydrate (98%), iron(III) nitrate nonahydrate (98%), iridium(IV) oxide (99.99%), urea (99%), hexamethylenetetramine (99%), and potassium hydroxide (99.98%) were purchased from Alfa Aesar. Methanol, ethanol, acetone, and hydrochloric acid were purchased from Beijing Chemical Work Co. in analytic grade (AR). All chemicals were used as received without further purification. NF and Nafion (5 wt.%, DuPont) were purchased from commercial suppliers. To remove the surface oxidation layer, the NF substrate was sonicated in 3 M HCl for 15 min and subsequently washed with water and a mixture of ethanol and acetone (1:1 in volume) three times before use. Milli-Q ultrapure water (resistance of 18.2 MΩ·cm at 25 °C) was used for all experiments.

Preparation of Co_3O_4/NF: A modified hydrothermal and annealing approach was applied to prepare Co_3O_4 microwire arrays on NF (Co_3O_4/NF). In a typical procedure, a mixture of 4 mmol cobalt(II) nitrate hexahydrate and 240 mg urea was dissolved in 30 mL Milli-Q ultrapure water under continuous stirring until the formation of a clear solution. The solution was then transferred into a 50 mL Teflon-lined stainless autoclave with a piece of cleaned NF. The autoclave was locked tightly and maintained in an electric oven at 120 °C for 8 h, then naturally cooled down. The resulting purple materials on NF were washed with ethanol and water three times. After drying naturally, the materials were annealed under 300 °C for 2 h in an air atmosphere to achieve final Co_3O_4/NF. The morphology of Co_3O_4/NF was carefully regulated by adjusting the feeding amount of cobalt(II) nitrate hexahydrate from 3 to 5 mmol.

Preparation of FeCo LDH@Co_3O_4/NF and FeCo LDH@NF: A mixture of 2 mmol cobalt(II) nitrate hexahydrate, 0.5 mmol iron(III) nitrate nonahydrate, and 1,000 mg hexamethylenetetramine was dissolved in 30 mL methanol under continuous stirring until the formation of a clear solution. The solution was then transferred into a 50 mL Teflon-lined stainless autoclave with a piece of the aforementioned Co_3O_4/NF. The autoclave was locked tightly and maintained in an electric oven at 180 °C for 8 h, then naturally cooled down. The resulting brownish materials were washed with ethanol and water three times. The control sample FeCo LDH@NF was synthesized using the same procedure except for replacing Co_3O_4/NF with NF.

Material characterizations: A Rigaku D/max 2500 with a Cu $K\alpha 1$ radiation source (λ = 1.54056 Å) was used to collect the X-ray diffraction (XRD) data. The catalyst structures were investigated via scanning electron microscopy (SEM, Hitachi SU-8020) at an accelerating voltage of 15 kV and a transmission electron microscopy (TEM, JEOL, JEM-2100F) at an acceleration voltage of 200 kV. Energy-dispersive X-ray spectra (EDS) were collected on an Oxford Materials Analysis EDS equipped on the TEM. The surface chemical bonding states of the samples were analyzed via X-ray photoelectron spectroscopy (XPS) using a Thermo Scientific ESCALab 250Xi with 300 W monochromatic Mg $K\alpha$ radiation.

First-principle calculation: First-principle calculations were performed with the Vienna *ab-initio* simulation package (VASP) [44]. We adopted the generalized gradient approximation (GGA) in the form of the Perdew–Burke–Ernzerhof (PBE) [45] for the exchange–correlation potentials. The projector augmented-wave (PAW) [46] pseudopotential was used with a plane-wave energy cutoff of 500 eV. Fe doped Co hydroxide was simulated by substituting one Co atom with a Fe atom in the 2 × 2 × 2 superlattice of Co hydroxide. Monkhorst–Pack [47] *k*-mesh of 9 × 9 × 5 was used for sampling the first Brillouin zone. The self-consistent field procedure was considered converged when the energy difference between two consecutive cycles was lower than 10^{-6} eV. Atomic positions and lattice parameters were relaxed until all the forces on the ions were less than 5×10^{-2} eV·Å^{-1}. The space group of the stimulated CoFe LDH was $P\bar{3}m1$, with cell parameters of *a*, *b*, and *c* being 3.163, 3.163, and 4.738 Å, respectively.

Electrochemical measurements: The electrochemical measurements were conducted on an Autolab PGSTAT302N (Metrohm, Netherlands) electrochemical workstation. A three-electrode configuration was assembled to evaluate the OER performance of the catalysts in 1 M KOH. The binder-free catalysts were directly applied as the working electrode. A carbon rod and an Ag/AgCl electrode were used as the counter and reference electrodes, respectively. The linear scanning voltammetry (LSV) polarization curves were recorded at a scan rate of 0.5 mV·s^{-1} with 90% *iR*-compensation. The chronopotentiometry (CP) curve was recorded at a constant current density of 50 mA·cm^{-2}. Electrochemical impedance spectroscopy (EIS) measurements were conducted under the potential of 1.64 V in the frequency range of 100 kHz to 10 mHz. All potentials reported in this work were referred to the reversible hydrogen electrode (vs. RHE), which was converted according to the Nernst equation.

Overall water splitting electrolyzer: The overall water splitting measurements were performed in a two-electrode system consisting of FeCo LDH@Co_3O_4/NF as the anode and $MoNi_4/MoO_2$/NF cathode prepared according to Refs. [48, 49]. The solar-driven water splitting system was assembled with a commercial GaAs solar cell without external bias. The solar simulator used in the experiment was Oriel Sol1A™ ABB-94021A with a Xenon lamp. The solar cell was placed under a simulated AM 1.5G 100 mW·cm^{-2} illumination to power the electrolyzer. The efficiency of solar to hydrogen conversion (STH) was calculated according to the following formula

$$\mathrm{STH} = \frac{1.23 \times j}{P} \times 100\%$$

where *j* is the current density and *P* is the light power density.

3 Results and discussion

The FeCo LDH@Co_3O_4/NF hierarchical structure was synthesized through a simple two-step hydrothermal procedure as illustrated in Fig. 1 (details see Experimental section). The vertically aligned Co_3O_4 microwire arrays were first fabricated on NF substrate (Co_3O_4/NF) as the mainstay via hydrothermal processing followed by annealing treatment. Subsequently, the nanosized FeCo LDH nanosheet arrays were grown onto the Co_3O_4 microwires (route 2 in Fig. 1). In contrast, without the participation of trivalent Fe^{3+} cations, the Co hydroxide grew in a form of large nanosheets over the Co_3O_4 microwire arrays and the hierarchical structure could not be achieved (route 1 in Fig. 1).

The crystal structure of the synthesized catalysts was probed by the XRD technique (Fig. S1 in the Electronic Supplementary Material (ESM)). Two intense typical diffraction peaks of NF substrate are marked by triangles. Co_3O_4/NF exhibits diffraction peaks that can be well indexed to the pure Co_3O_4 phase (JCPDS No. 42-1467). The diffraction peaks of FeCo LDH/NF can be attributed to a typical hydrotalcite-like structure, which is similar to the classical LDH structure of $Mg_6Fe_2CO_3(OH)_{16}\cdot 4H_2O$ (JCPDS No. 86-0182). The hierarchical FeCo LDH@Co_3O_4/NF mainly shows a Co_3O_4 phase. The low diffraction intensity for the FeCo LDH phase in the hierarchical structure, as marked by the asterisks, should be ascribed to the ultrathin and low crystalline nature of nanosheets as evidenced below.

The SEM images (Figs. 2(a) and 2(b)) reveal a lawn-like morphology of Co_3O_4/NF, inheriting from the original Co hydroxide/NF precursor (Fig. S2 in the ESM). These Co_3O_4 microwires are firmly attached to the NF substrate. No cracks are observed on the entire three-dimensional (3D) NF substrate (Fig. 2(a) and Fig. S3 in the ESM). It should be noted that such morphology of the Co_3O_4 microwire mainstay has been carefully regulated. The optimal Co_3O_4 microwires exhibit an average length of ~ 10 μm and a diameter of less than 300 nm (Fig. 2(b)). The longer microwires allow accommodating more LDH sub-architecture while too longer microwires tend to overlap at the end (Fig. S4 in the ESM). A smooth Co_3O_4 wire surface can be observed through the high-resolution SEM image (inset in Fig. 2(b)). Moreover, the TEM image (Fig. 2(c)) reveals a polycrystalline structure inside. A high-resolution TEM (HRTEM) image taken on the microwire (Fig. S5 in the ESM) displays clear lattice fringes with a *d* spacing of 0.21 nm corresponding to the (400) plane of Co_3O_4, corroborating it is Co_3O_4.

The binary FeCo LDH nanosheet substructure was further integrated onto the Co_3O_4 microwires via mild hydrothermal processing. As seen in SEM images (Figs. 2(d) and 2(e)), these FeCo LDH nanosheets are uniformly grown on the Co_3O_4 microwire surface while preserving their original lawn-like morphology. A curly nanosheet morphology with an average size of around 100 nm can be clearly observed in a TEM image (Fig. 2(f)). HRTEM image reveals that the FeCo LDH nanosheet is low crystalline (Fig. 2(g) and Fig. S6 in the ESM). The distinct lattice fringes with an interplanar spacing of 0.23 nm are the characteristic of the (015) plane of the LDH structure. Selective area electron diffraction (SAED) patterns of the FeCo LDH in Fig. 2(h) show obvious diffraction rings, confirming the low crystalline nature of the nanosheet, which is consistent with the XRD results. The marked representative rings can be indexed to the (015), (018), and (116) planes of FeCo LDH, respectively. Such a defect-rich structure could greatly enhance the surface area of the nanosheet and thus expose abundant active sites for catalyzing OER. The uniform distribution of elements Co, Fe, and O in the hierarchical structure is verified by the EDS mapping images (Fig. 2(i)). Notably, when lowering the Fe^{3+} salt concentration from 0.5 to 0.3 mmol, the FeCo LDH grows into larger nanosheets and partially blocks the interspace of original lawn-like Co_3O_4 arrays (Fig. S7 in the ESM). Furthermore, when Co^{2+} salt is only added as the metal source (without the addition of Fe^{3+} salt), the Co LDH grows in a form of large nanosheets above the original Co_3O_4 array, forming a top layer (Fig. S8 in the ESM). The hierarchical structure could not be achieved. This observation indicates that Fe^{3+} species play an important role in the formation of the hierarchical structure. In order to understand the underlying formation mechanism of the Fe^{3+} induced nanosizing effect of the LDH nanosheets, we have simulated Fe^{3+} doped and undoped Co hydroxide layer structure (denoted as Fe-$Co(OH)_2$ and $Co(OH)_2$, respectively) as shown in Figs. S9 and S10 in the ESM, for the LDH and metal hydroxides sharing a similar layer structure. The M^{3+} ions are atomically isolated by M^{2+} sites due to static repulsions, it is forbidden to form Fe^{3+}-O-Fe^{3+} motif inside the LDH layer [21]. Hence, in the modeling, each Fe^{3+} octahedra is surrounded by six Co^{2+} octahedra (Fig. S9 in the ESM). According to the crystal field theory, in metal-O octahedra of metal hydroxides, the valence electronic configurations of Co^{2+} and Fe^{3+} are $3d^7(t_{2g}^5 e_g^2)$ and $3d^5(t_{2g}^3 e_g^2)$, respectively [50, 51]. The Co^{2+} with one unpaired electron and two pairs of fully occupied electrons in the t_{2g} d orbital can be identified in a high-spin state (Co^{2+}-hs)

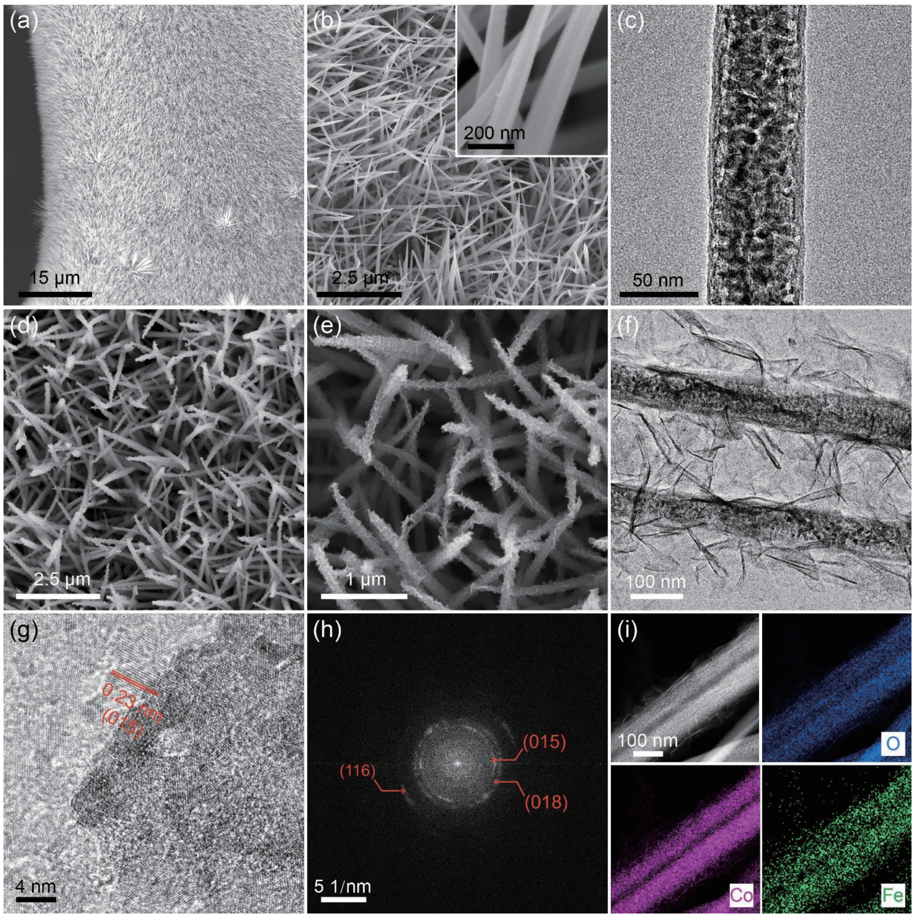

Figure 2 (a) and (b) SEM images at various magnifications and (c) TEM image of Co_3O_4 microwire. (d)–(e) SEM images at various magnifications, (f) TEM image, (g) HRTEM image, (h) SAED pattern, and (i) EDS mapping images of FeCo LDH/Co_3O_4/NF nanosheet-on-microwire hierarchical structure.

while the Fe^{3+} with three unpaired electrons in the t_{2g} d orbital in a low-spin state (Fe^{3+}-ls). The ion radius of Co^{2+}-hs is 74.5 pm while that of Fe^{3+}-ls is 55 pm [52]. It is found that introducing such Fe^{3+} cations with a small ion radius and high electrical repulsion would distort the neighboring Co^{2+} octahedra, thus leading to a deformed and unstable LDH layer structure. The optimized Fe-O octahedra in Fe-$Co(OH)_2$ shows a Fe–O bond length of 2.102 Å (Figs. S10(a) and S10(b) in the ESM), smaller than the Co–O bond length of 2.121 Å in Co-O octahedra in undoped $Co(OH)_2$ (Fig. S10(c) in the ESM). This suggests the distortion of Co-O octahedra after Fe^{3+} doping, which can be further evidenced by the different O–metal–O bond angles (83.892° and 96.108°) compared with that in Co-O octahedra (82.548° and 97.452°). More importantly, such deformed Fe-O octahedra significantly influences the neighboring Co-O octahedra. The Co–O bond length at the Co-O-Fe sharing edge of neighboring Co-O octahedra is 2.129 Å while it is 2.108 Å at the Co-O-Co sharing edges. These asymmetry Co-O octahedra further distort the whole LDH layer structure. Such overall layer distortion would obstruct the growth of large nanosheets, leading to the smaller ones. To experimentally prove this point, we have prepared the powder state Co LDH and FeCo LDH. The SEM images of Co LDH and FeCo LDH under the same magnification showed distinct morphology (Fig. S11 in ESM). The Co LDH exhibited a large petaliform nanosheet morphology in size of 5 μm while the FeCo LDH showed a crossed morphology consisting of a tiny nanosheet in the size of 300 nm. This evidences that Fe doping can significantly reduce the LDH nanosheet size, consistent with the observations in NF-supported FeCo LDH@Co_3O_4/NF. The reduction of nanosheet size is also reflected in the XRD patterns (Fig. S12 in ESM). The intense diffraction peaks of Co LDH correspond to a good crystallization degree, meaning a well-grown morphology and thus a large nanosheet size. In contrast, the FeCo LDH showed much weak and broader diffraction peaks. Such weak diffraction peaks of FeCo LDH imply a poor crystallization, which can be attributed to the lattice distortion induced by Fe doping forbidding the formation of large well-crystallized nanosheets. The control sample of FeCo LDH nanosheet directly grown on NF substrate (denoted as FeCo LDH/NF) was also prepared as shown in Fig. S13 in the ESM, which also shows a small nanosheet size, confirming the above analysis. Compared to the FeCo LDH/NF, it is reasonably expected the hierarchical structure of FeCo LDH/Co_3O_4/NF would significantly increase the exposed surface area of highly catalytic active FeCo LDH constituents.

The surface state of FeCo LDH@Co_3O_4/NF was then probed through XPS measurement. As displayed in Fig. S14(a) in the ESM, the Co $2p_{3/2}$ spectrum can be deconvoluted into double spin-orbit doublets at 780.9 and 779.6 eV with two satellites, respectively, corresponding to the Co^{2+} and Co^{3+} [53, 54]. The Fe species mainly exists in the Fe^{3+} state as evidenced by the typical Fe^{3+} peak at 711.8 in Fe $2p_{3/2}$ spectrum (Fig. S14(b) in the ESM) [55, 56]. The O 1s spectrum (Fig. S14(c) in the ESM) exhibits an intense peak at 530.8 eV corresponding to the OH^- species. Another two inconspicuous peaks located at 528.3 and 533 eV can be attributed to the lattice O and the absorbed H_2O species on the surface, which is commonly seen in metal hydroxides materials [32, 57].

To demonstrate the merit of constructing a hierarchical structure in high-rate water oxidation, the OER performance was measured by directly applying the binder-free FeCo LDH@Co_3O_4/NF as the working electrode with 1 M KOH as the electrolyte. An Ag/AgCl electrode and a carbon rod were used as the reference electrode and counter electrode, respectively. Commercial IrO_2 catalyst was also coated on NF as the reference. Co_3O_4/NF catalyst without the secondary growth of FeCo LDH and FeCo LDH/NF catalyst directly grown on NF without Co_3O_4 microwire array were measured for comparison. The OER activities were first evaluated by the LSV curve with 90% *iR*-compensation. As shown in Fig. 3(a), the bare NF shows very poor activity for OER, indicating the contribution of NF to the overall OER current is negligible. The hierarchical structured FeCo LDH@Co_3O_4/NF exhibits a much higher OER current density than both Co_3O_4/NF and FeCo LDH/NF in the entire scanning range. Specifically, the FeCo LDH@Co_3O_4/NF delivers current densities of 10 and 100 mA·cm^{-2} at the lowest overpotentials of 226 and 297 mV, respectively (Fig. 3(a) and Fig. S15 in the ESM), outperforming that of Co_3O_4/NF (279 and 373 mV) and FeCo LDH/NF (238 and 338 mV). The such performance also outperforms commercial IrO_2 loaded on the NF (309 and 407 mV). The current density reaches 1,000 mA·cm^{-2} at a low overpotential of 392 mV, indicating the superior performance of FeCo LDH@Co_3O_4/NF under high-rate water oxidation.

To understand the origin of the superior OER catalytic performance of FeCo LDH@Co_3O_4/NF, a series of experiments were conducted. We have compared the OER performance of Co LDH/NF and FeCo LDH/NF (Fig. S16 in ESM). The FeCo LDH/NF showed a high OER performance compared to the Co LDH/NF even normalized by the electrochemical surface areas (ECSA), demonstrating the Fe dopant can tailor the electronic structure of Co sites to serve as high intrinsic OER sites. The ECSA of the NF-supported catalysts was then evaluated (Fig. 3(b) and Fig. S17 in the ESM). The hierarchical FeCo LDH@Co_3O_4/NF exhibits the largest value of 18.97 mF·cm^{-2}, which is 4.37 and 3.68 times higher than FeCo LDH/NF (4.34 mF·cm^{-2}) and Co_3O_4/NF (5.15 mF·cm^{-2}), respectively, indicating the advantage of constructing a hierarchical structure in the exposure of active sites. Furthermore, EIS analysis was applied to investigate the electron transfer kinetics during the OER process (Fig. 3(c)). All catalysts exhibit similar solution resistances (R_s) but significantly distinct charge transfer resistances (R_{ct}). The smallest value of FeCo LDH@Co_3O_4/NF reveals its fast electron transfer kinetics. It can be attributed to the Fe doping enhancing the electrical conductivity for electron hopping between different cations while the robust Co_3O_4 mainstay on NF provides an expressway for charge transfer during the reaction. Hence, the superior high-rate water oxidation performance of FeCo LDH@Co_3O_4/NF can be ascribed to: The densely grown FeCo LDH nanosheet substructures provide sufficient highly-active sites; the macropores of NF and open spacing between neighboring microwires facilitate electrolyte penetration and mass transport, and the Fe doping and Co_3O_4 mainstay improve the electron transport.

Besides the catalytic activity, the long-term OER durability of FeCo LDH@Co_3O_4/NF was evaluated under a fixed current density of 50 mA·cm^{-2}. The negligible change is observed after continuous operation for 30 h, suggesting its excellent durability (Fig. 3(d)), which can be attributed to the chemical durable FeCo LDH together with mechanical durable binder-free architecture. The SEM images of the FeCo LDH@Co_3O_4/NF after the durability test indicate that the hierarchical morphology is well maintained (Fig. S18 in the ESM). XPS measurements were also performed to investigate the structural evolution during the OER. As shown in Fig. S19 in the ESM, a part of Co^{2+} is converted into Co^{3+} while the Fe species maintains a trivalent state. The lattice O content is much enhanced after the durability tests, which can be attributed to the formation of amorphous metal oxyhydroxides during the OER process. This transformation is commonly reported for transitional-metal OER catalysts [58, 59]. The above results demonstrate that the construction of hierarchically structured FeCo LDH@Co_3O_4/NF with FeCo LDH nanosheets on Co_3O_4 microwire arrays is an effective strategy to boost OER activity while keeping the robust durability.

Inspired by the superior OER catalytic performance of FeCo LDH@Co_3O_4/NF, a practical two-electrode water electrolyzer was built to evaluate its performance in practical energy conventional devices. A previously reported $MoNi_4$ on MoO_2 rods grown on NF (denoted as $MoNi_4$/MoO_2/NF) was prepared according to the literature to serve as the cathode hydrogen evolution electrode [48, 49]. As shown in Fig. S20 in the ESM, the $MoNi_4$/MoO_2/NF can deliver a high current density of 100 mA·cm^{-2} with a low overpotential of 99 mV, indicating the excellent HER catalytic performance. The overall water splitting curve of the two-electrode cell was measured as shown in Fig. 4(a). It only requires low cell voltages of 1.49 and 1.61 V to drive the water oxidation in current densities of 10 and 100 mA·cm^{-2}. The overall water oxidation current density can reach 0.34 A·cm^{-2} under a relatively low cell voltage of 1.80 V, implying the high-rate electrocatalytic capacity. Such performance outperforms most of the recently reported state-of-the-art analogs (Fig. 4(b) and Table S1 in the

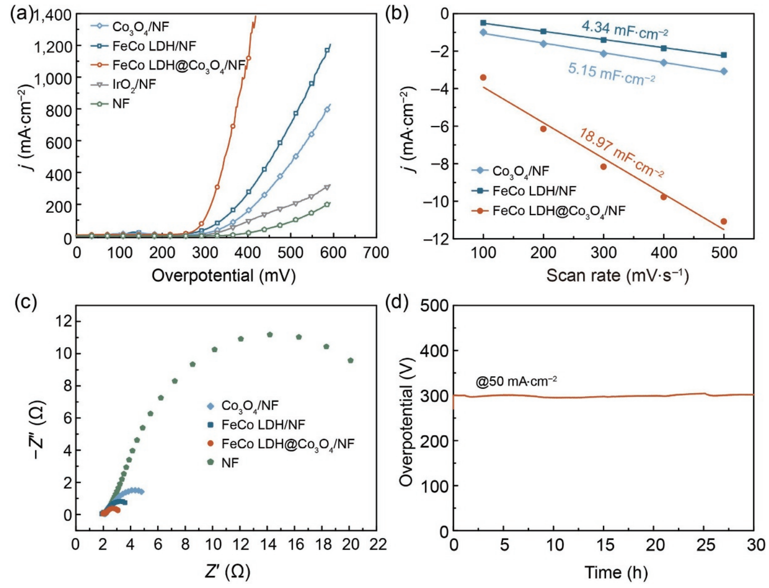

Figure 3 (a) Steady-state OER polarization curves at a sweep rate of 0.5 mV·s^{-1} with 90% *iR*-compensation, (b) current density as a function of scan rate, and (c) Nyquist plots of the as-prepared catalysts. (d) Chronopotentiometry curve recorded on FeCo LDH@Co_3O_4/NF at a constant current density of 50 mA·cm^{-2}.

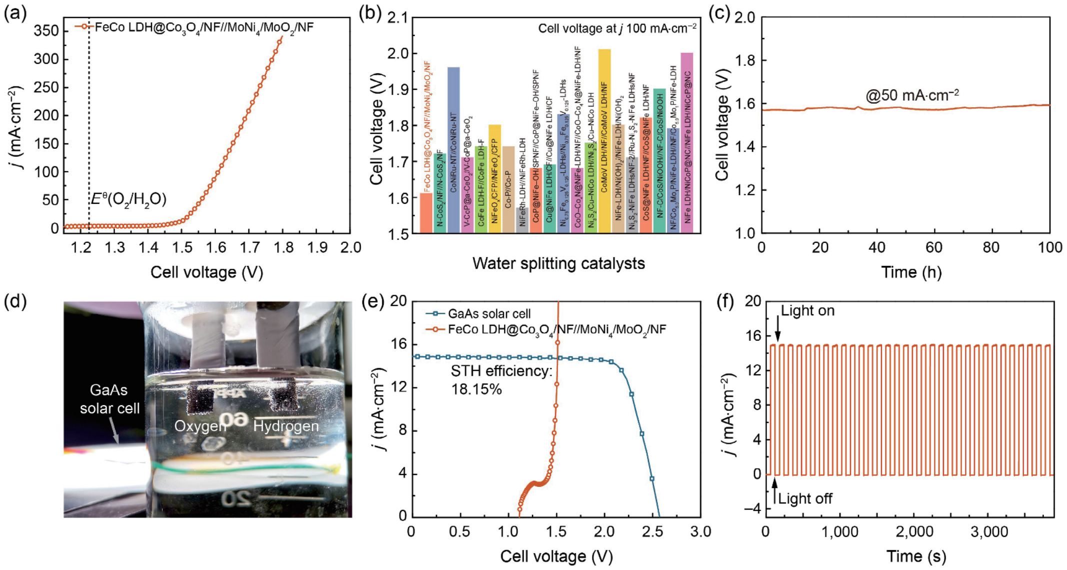

Figure 4 (a) Steady-state overall water splitting curve of FeCo LDH@Co_3O_4/NF//$MoNi_4$/MoO_2/NF electrolyzer. (b) A comparison of cell voltages for the present electrolyzer and reported ones at 100 mA·cm^{-2}. (c) Chronopotentiometry curve recorded at a constant current density of 50 mA·cm^{-2} of FeCo LDH@Co_3O_4/NF//$MoNi_4$/MoO_2/NF electrolyzer. (d) The optical image, (e) *J*–*V* curves, and (f) time-dependent current output of the assembled solar-driven electrolyzer without external bias.

ESM) [26, 60–63]. The long-term durability was also evaluated. The cell voltage remains steadily at the current density of 50 mA·cm^{-2} for 100 h (Fig. 4(c)). Furthermore, the electrolyzer was further integrated with a commercial GaAs solar cell to demonstrate a solar-driven water-splitting system, as shown in Fig. 4(d). The system was placed under an AM 1.5G 100 mW·cm^{-2} solar simulator with a Xenon lamp (Fig. S21 in the ESM). The *J*–*V* curves (Fig. 4(e)) present a high solar-to-hydrogen efficiency of 18.15% with continuous oxygen and hydrogen production on the electrodes (Fig. 4(d)), which is ranking the top class of the analogs. To investigate the anti-fluctuation ability of the assembled system, a time-dependent experiment with periodic light turn-on and -off was performed. The system exhibits a steady output and good light response in a near 4,000 s operation (Fig. 4(f)), demonstrating the potential application of the reported FeCo LDH@Co_3O_4/NF in the practical solar-driven water-splitting system.

4 Conclusions

In summary, a Fe^{3+} induced nanosizing strategy was developed to successfully construct a hierarchical structure of FeCo LDH nanosheet arrays on Co_3O_4 microwire arrays as a binder-free electrode to boost the high-rate water oxidation. It was found that the Fe^{3+} substitution not only created intrinsically highly-active OER sites via electronic modulation of Co center but also significantly reduced the nanosheet size of LDHs, enabling the formation of a "nanosheet-on-microwire" hierarchical structure which could not be achieved without the participation of Fe^{3+}. Density functional theory (DFT) simulations indicated that the introduction of trivalent Fe^{3+} cations with small ion radius and high electrical repulsion in the LDH layer led to the structural distortion of M-O_6 octahedra, resulting in reduced nanosheet size. Benefiting from the significantly enhanced electrochemical surface areas and charge/mass transport due to the hierarchical structure together with the highly-active OER sites, such FeCo LDH@Co_3O_4 nanosheet-on-microwire electrode exhibited much improved OER catalytic performance. It required small overpotentials of 226 and 392 mV to deliver the current density of 10 and 1,000 mA·cm^{-2}, respectively. When assembled in a practical electrolyzer, a water splitting current density of 100 mA·cm^{-2} could be achieved at a low operation voltage of 1.61 V with excellent durability. Powered by solar light, a solar-to-hydrogen efficiency of 18.15% was also demonstrated with steady photoresponse. These results might open up an avenue for constructing hierarchically structured micro/nanohybrid composites for advanced water electrolysis and diverse applications.

Acknowledgements

The authors acknowledge the financial support from the National Natural Science Foundation of China (Nos. 22025208, 22075300, and 21902162), the China National Postdoctoral Program for Innovative Talents (No. BX2021319), the DNL Cooperation Fund, CAS (No. DNL202008), and the Chinese Academy of Sciences. We also thank Dr. Z.-J. Z., X.-Y. Z., and B.-L. Q. for the XPS analysis; Y. S. for the XRD analysis; and Dr. B. G., Y.-X. C., and J.-L. Y. for SEM and TEM support.

Electronic Supplementary Material: Supplementary material (XRD patterns, SEM images, TEM images, XPS spectra, electrochemical measurements, and supplementary tables) is available in the online version of this article at https://doi.org/10.1007/s12274-022-5094-8.

References

[1] Lagadec, M. F.; Grimaud, A. Water electrolysers with closed and open electrochemical systems. *Nat. Mater.* **2020**, *19*, 1140–1150.

[2] Logan, B. E.; Elimelech, M. Membrane-based processes for sustainable power generation using water. *Nature* **2012**, *488*, 313–319.

[3] Zhao, L.; Zhang, Y.; Zhao, Z. L.; Zhang, Q. H.; Huang, L. B.; Gu, L.; Lu, G.; Hu, J. S.; Wan, L. J. Steering elementary steps towards efficient alkaline hydrogen evolution via size-dependent Ni/NiO nanoscale heterosurfaces. *Natl. Sci. Rev.* **2020**, *7*, 27–36.

[4] Li, J. H.; Wang, L. J.; He, H. J.; Chen, Y. Q.; Gao, Z. R.; Ma, N.; Wang, B.; Zheng, L. L.; Li, R. L.; Wei, Y. J. et al. Interface construction of NiCo LDH/NiCoS based on the 2D ultrathin nanosheet towards oxygen evolution reaction. *Nano Res.* **2022**, *15*, 4986–4995.

[5] Zhu, Y. P.; Guo, C. X.; Zheng, Y.; Qiao, S. Z. Surface and interface engineering of noble-metal-free electrocatalysts for efficient energy conversion processes. *Acc. Chem. Res.* **2017**, *50*, 915–923.

[6] Zhang, B.; Zheng, X. L.; Voznyy, O.; Comin, R.; Bajdich, M.; García-Melchor, M.; Han, L. L.; Xu, J. X.; Liu, M.; Zheng, L. R. et al. Homogeneously dispersed multimetal oxygen-evolving catalysts. *Science* **2016**, *352*, 333–337.

[7] Che, Z. W.; Lu, X. Y.; Cai, B. F.; Xu, X. X.; Bao, J. C.; Liu, Y. Ligand-controlled synthesis of high density and ultra-small Ru nanoparticles with excellent electrocatalytic hydrogen evolution performance. *Nano Res.* **2022**, *15*, 1269–1275.

[8] Rausch, B.; Symes, M. D.; Chisholm, G.; Cronin, L. Decoupled catalytic hydrogen evolution from a molecular metal oxide redox mediator in water splitting. *Science* **2014**, *345*, 1326–1330.

[9] Tang, T.; Jiang, W. J.; Niu, S.; Liu, N.; Luo, H.; Chen, Y. Y.; Jin, S. F.; Gao, F.; Wan, L. J.; Hu, J. S. Electronic and morphological dual modulation of cobalt carbonate hydroxides by Mn doping toward highly efficient and stable bifunctional electrocatalysts for overall water splitting. *J. Am. Chem. Soc.* **2017**, *139*, 8320–8328.

[10] Wang, T. H.; Tao, L.; Zhu, X. R.; Chen, C.; Chen, W.; Du, S. Q.; Zhou, Y. Y.; Zhou, B.; Wang, D. D.; Xie, C. et al. Combined anodic and cathodic hydrogen production from aldehyde oxidation and hydrogen evolution reaction. *Nat. Catal.* **2022**, *5*, 66–73.

[11] Zhang, Q.; Chen, H.; Yang, L.; Liang, X.; Shi, L.; Feng, Q.; Zou, Y. C.; Li, G. D.; Zou, X. X. Non-catalytic, instant iridium(Ir) leaching: A non-negligible aspect in identifying Ir-based perovskite oxygen-evolving electrocatalysts. *Chin. J. Catal.* **2022**, *43*, 885–893.

[12] Yang, L.; Zhang, K. X.; Chen, H.; Shi, L.; Liang, X.; Wang, X. Y.; Liu, Y. P.; Feng, Q.; Liu, M. J.; Zou, X. X. An ultrathin two-dimensional iridium-based perovskite oxide electrocatalyst with highly efficient {001} facets for acidic water oxidation. *J. Energy Chem.* **2022**, *66*, 619–627.

[13] Zhao, S. L.; Wang, Y.; Dong, J. C.; He, C. T.; Yin, H. J.; An, P. F.; Zhao, K.; Zhang, X. F.; Gao, C.; Zhang, L. J. et al. Ultrathin metal–organic framework nanosheets for electrocatalytic oxygen evolution. *Nat. Energy* **2016**, *1*, 16184.

[14] Jiang, W. J.; Tang, T.; Zhang, Y.; Hu, J. S. Synergistic modulation of non-precious-metal electrocatalysts for advanced water splitting. *Acc. Chem. Res.* **2020**, *53*, 1111–1123.

[15] Yuan, L. P.; Wu, Z. Y.; Jiang, W. J.; Tang, T.; Niu, S.; Hu, J. S. Phosphorus-doping activates carbon nanotubes for efficient electroreduction of nitrogen to ammonia. *Nano Res.* **2020**, *13*, 1376–1382.

[16] Gong, M.; Dai, H. J. A mini review of NiFe-based materials as highly active oxygen evolution reaction electrocatalysts. *Nano Res.* **2015**, *8*, 23–39.

[17] Yan, Y.; Liu, C. Y.; Jian, H. W.; Cheng, X.; Hu, T.; Wang, D.; Shang, L.; Chen, G.; Schaaf, P.; Wang, X. Y. et al. Substitutionally dispersed high-oxidation CoO_x clusters in the lattice of rutile TiO_2 triggering efficient Co-Ti cooperative catalytic centers for oxygen evolution reactions. *Adv. Funct. Mater.* **2021**, *31*, 2009610.

[18] Roger, I.; Shipman, M. A.; Symes, M. D. Earth-abundant catalysts for electrochemical and photoelectrochemical water splitting. *Nat. Rev. Chem.* **2017**, *1*, 0003.

[19] Niu, S.; Jiang, W. J.; Tang, T.; Yuan, L. P.; Luo, H.; Hu, J. S. Autogenous growth of hierarchical $NiFe(OH)_x$/FeS nanosheet-on-microsheet arrays for synergistically enhanced high-output water oxidation. *Adv. Funct. Mater.* **2019**, *29*, 1902180.

[20] Luo, Y. T.; Zhang, Z. Y.; Chhowalla, M.; Liu, B. L. Recent advances in design of electrocatalysts for high-current-density water splitting. *Adv. Mater.* **2022**, *34*, 2108133.

[21] Cai, Z.; Zhou, D. J.; Wang, M. Y.; Bak, S. M.; Wu, Y. S.; Wu, Z. S.; Tian, Y.; Xiong, X. Y.; Li, Y. P.; Liu, W. et al. Introducing Fe^{2+} into nickel-iron layered double hydroxide: Local structure modulated water oxidation activity. *Angew. Chem., Int. Ed.* **2018**, *57*, 9392–9396.

[22] Li, H. Y.; Chen, S. M.; Zhang, Y.; Zhang, Q. H.; Jia, X. F.; Zhang, Q.; Gu, L.; Sun, X. M.; Song, L.; Wang, X. Systematic design of superaerophobic nanotube-array electrode comprised of transition-metal sulfides for overall water splitting. *Nat. Commun.* **2018**, *9*, 2452.

[23] Pham, C. V.; Escalera-López, D.; Mayrhofer, K.; Cherevko, S.; Thiele, S. Essentials of high performance water electrolyzers-from catalyst layer materials to electrode engineering. *Adv. Energy Mater.* **2021**, *11*, 2101998.

[24] Park, S.; Shao, Y. Y.; Liu, J.; Wang, Y. Oxygen electrocatalysts for water electrolyzers and reversible fuel cells: Status and perspective. *Energy Environ. Sci.* **2012**, *5*, 9331–9344.

[25] Liu, Y. P.; Liang, X.; Gu, L.; Zhang, Y.; Li, G. D.; Zou, X. X.; Chen, J. S. Corrosion engineering towards efficient oxygen evolution electrodes with stable catalytic activity for over 6,000 hours. *Nat. Commun.* **2018**, *9*, 2609.

[26] Niu, S.; Jiang, W. J.; Wei, Z. X.; Tang, T.; Ma, J. M.; Hu, J. S.; Wan, L. J. Se-doping activates FeOOH for cost-effective and efficient electrochemical water oxidation. *J. Am. Chem. Soc.* **2019**, *141*, 7005–7013.

[27] Xiao, C. L.; Li, Y. B.; Lu, X. Y.; Zhao, C. Bifunctional porous $NiFe/NiCo_2O_4/Ni$ foam electrodes with triple hierarchy and double synergies for efficient whole cell water splitting. *Adv. Funct. Mater.* **2016**, *26*, 3515–3523.

[28] Dong, X. W.; Zhang, Y. Q.; Song, M. L.; Tao, S. S.; Wang, H. F.; Zhou, P.; Wang, D. D.; Wu, Y. J.; Chen, C. M.; Su, C. L. et al. Colloid self-assembly of *c*-axis oriented hydroxide thin films to boost the electrocatalytic oxidation reaction. *Chem. Eng. J.* **2021**, *420*, 130532.

[29] Liu, X. Z.; Tang, T.; Jiang, W. J.; Zhang, Q. H.; Gu, L.; Hu, J. S. Fe-doped Co_3O_4 polycrystalline nanosheets as a binder-free bifunctional cathode for robust and efficient zinc-air batteries. *Chem. Commun.* **2020**, *56*, 5374–5377.

[30] Wu, J.; Ren, Z. Y.; Du, S. C.; Kong, L. J.; Liu, B. W.; Xi, W.; Zhu, J. Q.; Fu, H. G. A highly active oxygen evolution electrocatalyst: Ultrathin CoNi double hydroxide/CoO nanosheets synthesized via interface-directed assembly. *Nano Res.* **2016**, *9*, 713–725.

[31] Song, F.; Hu, X. L. Exfoliation of layered double hydroxides for enhanced oxygen evolution catalysis. *Nat. Commun.* **2014**, *5*, 4477.

[32] Qian, L.; Lu, Z. Y.; Xu, T. H.; Wu, X. C.; Tian, Y.; Li, Y. P.; Huo, Z. Y.; Sun, X. M.; Duan, X. Trinary layered double hydroxides as high-performance bifunctional materials for oxygen electrocatalysis. *Adv. Energy Mater.* **2015**, *5*, 1500245.

[33] Yin, P. Q.; Wu, G.; Wang, X. Q.; Liu, S. J.; Zhou, F. Y.; Dai, L.; Wang, X.; Yang, B.; Yu, Z. Q. NiCo-LDH nanosheets strongly coupled with GO-CNTs as a hybrid electrocatalyst for oxygen evolution reaction. *Nano Res.* **2021**, *14*, 4783–4788.

[34] Jia, X. D.; Zhang, X.; Zhao, J. Q.; Zhao, Y. F.; Zhao, Y. X.; Waterhouse, G. I. N.; Shi, R.; Wu, L. Z.; Tung, C. H.; Zhang, T. R. Ultrafine monolayer Co-containing layered double hydroxide nanosheets for water oxidation. *J. Energy Chem.* **2019**, *34*, 57–63.

[35] Zhang, X.; Zhao, Y. F.; Zhao, Y. X.; Shi, R.; Waterhouse, G. I. N.; Zhang, T. R. A simple synthetic strategy toward defect-rich porous monolayer NiFe-layered double hydroxide nanosheets for efficient electrocatalytic water oxidation. *Adv. Energy Mater.* **2019**, *9*, 1900881.

[36] Chen, W.; Wang, Y. Y.; Wu, B. B.; Shi, J. Q.; Li, Y. Y.; Xu, L. T.; Xie, C.; Zhou, W.; Huang, Y. C.; Wang, T. H. et al. Activated Ni–OH bonds in a catalyst facilitates the nucleophile oxidation reaction. *Adv. Mater.* **2022**, *34*, 2105320.

[37] Li, R. Q.; Liu, Y. Q.; Li, H. B.; Zhang, M.; Lu, Y. R.; Zhang, L.; Xiao, J. P.; Boehm, F.; Yan, K. One-step synthesis of NiMn-layered double hydroxide nanosheets efficient for water oxidation. *Small Methods* **2019**, *3*, 1800344.

[38] Kang, Y.; Wang, S.; Hui, K. S.; Wu, S. X.; Dinh, D. A.; Fan, X.; Bin, F.; Chen, F. M.; Geng, J. X.; Cheong, W. C. M. et al. Surface reconstruction establishing mott-schottky heterojunction and built-in space-charging effect accelerating oxygen evolution reaction. *Nano Res.* **2022**, *15*, 2952–2960.

[39] Zhao, Y. X.; Zheng, L. R.; Shi, R.; Zhang, S.; Bian, X. A.; Wu, F.; Cao, X. Z.; Waterhouse, G. I. N.; Zhang, T. R. Alkali etching of layered double hydroxide nanosheets for enhanced photocatalytic N_2 reduction to NH_3. *Adv. Energy Mater.* **2020**, *10*, 2002199.

[40] McCrory, C. C. L.; Jung, S.; Ferrer, I. M.; Chatman, S. M.; Peters, J. C.; Jaramillo, T. F. Benchmarking hydrogen evolving reaction and oxygen evolving reaction electrocatalysts for solar water splitting devices. *J. Am. Chem. Soc.* **2015**, *137*, 4347–4357.

[41] Long, X.; Li, J. K.; Xiao, S.; Yan, K. Y.; Wang, Z. L.; Chen, H. N.; Yang, S. H. A strongly coupled graphene and FeNi double hydroxide

hybrid as an excellent electrocatalyst for the oxygen evolution reaction. *Angew. Chem., Int. Ed.* **2014**, *53*, 7584–7588.

[42] Zhao, Z. Y.; Shao, Q.; Xue, J. Y.; Huang, B. L.; Niu, Z.; Gu, H. W.; Huang, X. Q.; Lang, J. P. Multiple structural defects in ultrathin NiFe-LDH nanosheets synergistically and remarkably boost water oxidation reaction. *Nano Res.* **2022**, *15*, 310–316.

[43] Peng, L. S.; Yang, N.; Yang, Y. Q.; Wang, Q.; Xie, X. Y.; Sun-Waterhouse, D.; Shang, L.; Zhang, T. R.; Waterhouse, G. I. N. Atomic cation-vacancy engineering of NiFe-layered double hydroxides for improved activity and stability towards the oxygen evolution reaction. *Angew. Chem., Int. Ed.* **2021**, *60*, 24612–24619.

[44] Kresse, G.; Furthmüller, J. Efficiency of *ab-initio* total energy calculations for metals and semiconductors using a plane-wave basis set. *Comput. Mater. Sci.* **1996**, *6*, 15–50.

[45] Perdew, J. P.; Burke, K.; Ernzerhof, M. Generalized gradient approximation made simple. *Phys. Rev. Lett.* **1996**, *77*, 3865–3868.

[46] Kresse, G.; Joubert, D. From ultrasoft pseudopotentials to the projector augmented-wave method. *Phys. Rev. B* **1999**, *59*, 1758–1775.

[47] Monkhorst, H. J.; Pack, J. D. Special points for brillouin-zone integrations. *Phys. Rev. B* **1976**, *13*, 5188–5192.

[48] Zhang, J.; Wang, T.; Liu, P.; Liao, Z. Q.; Liu, S. H.; Zhuang, X. D.; Chen, M. W.; Zschech, E.; Feng, X. L. Efficient hydrogen production on $MoNi_4$ electrocatalysts with fast water dissociation kinetics. *Nat. Commun.* **2017**, *8*, 15437.

[49] Chen, Y. Y.; Zhang, Y.; Zhang, X.; Tang, T.; Luo, H.; Niu, S.; Dai, Z. H.; Wan, L. J.; Hu, J. S. Self-templated fabrication of $MoNi_4/MoO_{3-x}$ nanorod arrays with dual active components for highly efficient hydrogen evolution. *Adv. Mater.* **2017**, *29*, 1703311.

[50] Kong, F. H.; Zhang, W. W.; Sun, L. P.; Huo, L. H.; Zhao, H. Interface electronic coupling in hierarchical FeLDH(FeCo)/Co$(OH)_2$ arrays for efficient electrocatalytic oxygen evolution. *ChemSusChem* **2019**, *12*, 3592–3601.

[51] Ejaz, A.; Jeon, S. Synthesis and application of electrochemically reduced N-rGO-Co$(OH)_2$ nanocomposite for concurrent detection of biomolecules. *Electrochim. Acta* **2017**, *235*, 709–719.

[52] Shannon, R. D. Revised effective ionic radii and systematic studies of interatomic distances in halides and chalcogenides. *Acta Crystallogr., Sect. A: Cryst. Phys., Diffr., Theor. Gen. Crystallogr.* **1976**, *32*, 751–767.

[53] Zhao, S.; Jin, R. X.; Abroshan, H.; Zeng, C. J.; Zhang, H.; House, S. D.; Gottlieb, E.; Kim, H. J.; Yang, J. C.; Jin, R. C. Gold nanoclusters promote electrocatalytic water oxidation at the nanocluster/$CoSe_2$ interface. *J. Am. Chem. Soc.* **2017**, *139*, 1077–1080.

[54] Gu, D.; Jia, C. J.; Weidenthaler, C.; Bongard, H. J.; Spliethoff, B.; Schmidt, W.; Schüth, F. Highly ordered mesoporous cobalt-containing oxides: Structure, catalytic properties, and active sites in oxidation of carbon monoxide. *J. Am. Chem. Soc.* **2015**, *137*, 11407–11418.

[55] Wang, Q.; Shang, L.; Shi, R.; Zhang, X.; Zhao, Y. F.; Waterhouse, G. I. N.; Wu, L. Z.; Tung, C. H.; Zhang, T. R. NiFe layered double hydroxide nanoparticles on Co, N-codoped carbon nanoframes as efficient bifunctional catalysts for rechargeable zinc-air batteries. *Adv. Energy Mater.* **2017**, *7*, 1700467.

[56] Tang, T.; Jiang, W. J.; Niu, S.; Yuan, L. P.; Hu, J. S.; Wan, L. J. Hetero-coupling of a carbonate hydroxide and sulfide for efficient and robust water oxidation. *J. Mater. Chem. A* **2019**, *7*, 21959–21965.

[57] Jia, Y.; Zhang, L. Z.; Gao, G. P.; Chen, H.; Wang, B.; Zhou, J. Z.; Soo, M. T.; Hong, M.; Yan, X. C.; Qian, G. R. et al. A heterostructure coupling of exfoliated Ni-Fe hydroxide nanosheet and defective graphene as a bifunctional electrocatalyst for overall water splitting. *Adv. Mater.* **2017**, *29*, 1700017.

[58] Zhang, J. F.; Liu, J. Y.; Xi, L. F.; Yu, Y. F.; Chen, N.; Sun, S. H.; Wang, W. C.; Lange, K. M.; Zhang, B. Single-atom Au/NiFe layered double hydroxide electrocatalyst: Probing the origin of activity for oxygen evolution reaction. *J. Am. Chem. Soc.* **2018**, *140*, 3876–3879.

[59] Wu, T. Z.; Sun, S. N.; Song, J. J.; Xi, S. B.; Du, Y. H.; Chen, B.; Sasangka, W. A.; Liao, H. B.; Gan, C. L.; Scherer, G. G. et al. Iron-facilitated dynamic active-site generation on spinel $CoAl_2O_4$ with self-termination of surface reconstruction for water oxidation. *Nat. Catal.* **2019**, *2*, 763–772.

[60] Yao, N.; Li, P.; Zhou, Z. R.; Meng, R.; Cheng, G. Z.; Luo, W. Nitrogen engineering on 3D dandelion-flower-like CoS_2 for high-performance overall water splitting. *Small* **2019**, *15*, 1901993.

[61] Wang, Y.; Wang, S.; Ma, Z. L.; Yan, L. T.; Zhao, X. B.; Xue, Y. Y.; Huo, J. M.; Yuan, X.; Li, S. N.; Zhai, Q. G. Competitive coordination-oriented monodispersed ruthenium sites in conductive MOF/LDH hetero-nanotree catalysts for efficient overall water splitting in alkaline media. *Adv. Mater.* **2022**, *34*, 2107488.

[62] Zhang, H. J.; Li, X. P.; Hähnel, A.; Naumann, V.; Lin, C.; Azimi, S.; Schweizer, S. L.; Maijenburg, A. W.; Wehrspohn, R. B. Bifunctional heterostructure assembly of NiFe LDH nanosheets on NiCoP nanowires for highly efficient and stable overall water splitting. *Adv. Funct. Mater.* **2018**, *28*, 1706847.

[63] Huang, Y.; Wang, J. J.; Zou, Y.; Jiang, L. W.; Liu, X. L.; Jiang, W. J.; Liu, H.; Hu, J. S. Selective Se doping of $NiFe_2O_4$ on an active NiOOH scaffold for efficient and robust water oxidation. *Chin. J. Catal.* **2021**, *42*, 1395–1403.